

Ultrafast coherent nonlinear nanooptics and nanoimaging of graphene

Tao Jiang^{1,2}, Vasily Kravtsov^{1,2,3}, Mikhail Tokman⁴, Alexey Belyanin^{5*} and Markus B. Raschke^{1,2*}

With its linear energy dispersion and large transition dipole matrix element, graphene is an attractive material for nonlinear optoelectronic applications. However, the mechanistic origin of its strong nonlinear response, the ultrafast coherent dynamics and the associated nanoscale phenomena have remained elusive due to a lack of suitable experimental techniques. Here, using adiabatic nanofocusing and imaging, we study the broadband four-wave mixing (FWM) response of graphene with nanometre and femtosecond spatio-temporal resolution. We detect a nonlinear signal enhancement at the edges and dependence on the number of layers from excitation areas as small as 10^4 carbon atoms. Femtosecond FWM nanoimaging and concomitant frequency-domain measurements reveal dephasing on $T_2 \approx 6 \pm 1$ fs timescales, which we attribute to a strong electron–electron interaction. We also identify an unusual non-local FWM response on ~ 100 – 400 nm length scales, which we assign to a Doppler effect controlling the nonlinear interaction between the tip near-field momenta and the graphene electrons with high Fermi velocity. These results illustrate the distinct nonlinear nanooptical properties of graphene, expected also in related classes of two-dimensional materials, that could form the basis for improved nonlinear and ultrafast nanophotonic devices.

Graphene is one of the most remarkable nonlinear optical materials, with strong and broadband nonlinear properties due to its gapless electronic band structure with a linear electronic dispersion near its Dirac points^{1,2}. This, together with other unique properties such as high thermal conductivity and carrier mobility and a strong interaction with photons ranging from the terahertz to the ultraviolet^{3–7}, make graphene a material of choice for future nonlinear frequency conversion, all-optical control and information processing.

An even-order nonlinear response is generally forbidden in graphene because of its inversion symmetry^{1,2}, so this response is only observed beyond the electric dipole approximation^{8–10} or in the presence of electric fields and currents or layer-stacking effects^{11–14}. However, third and higher odd-order processes are electric-dipole-allowed, with strong coherent four-wave mixing (FWM)^{15–18} and third^{19–23} and higher harmonic generation^{24,25}, demonstrating efficient, broadband and electrically tunable nonlinearities.

Despite the large value of the third-order nonlinear susceptibility, $\chi^{(3)}$, of graphene because of its large optical transition dipole matrix element of $\sim e v_F / \omega$, the nonlinear response is signal-limited by the two-dimensional (2D) interaction volume. Theoretically suggested approaches to enhance the graphene nonlinear signal include the use of quantum confinement in nanostructures²⁶, localized plasmonic resonances^{27,28} and specially designed layered structures²⁹. However, graphene nonlinearities under nanolocalized optical excitation, their coherence properties and their dependence on edge, layer and other finite size effects have not yet been studied because of the lack of suitable experimental techniques.

In this Article, we demonstrate a new approach towards coherent nonlinear nanoimaging and nanospectroscopy of graphene through near-field excitation, based on adiabatic plasmonic nanofocusing of ultrashort few-femtosecond laser pulses for nanoconfined spatio-temporal excitation and imaging^{30–34}. FWM experiments were

performed as illustrated in Fig. 1a (see Methods for details), with the tip in atomic-force-controlled interaction with exfoliated graphene on a SiO₂/Si substrate.

Near-field graphene FWM

Due to the gradient field effect at the gold tip apex, nanoconfined surface plasmon polaritons (SPPs) generate efficient broadband intrapulse FWM in the gold itself, as demonstrated recently^{32,33} and shown for reference in Fig. 1b (blue). Despite a 3D volume effect within the metal of the tip apex of radius ~ 10 nm, the 2D graphene FWM response dominates the signal with the tip in near-field interaction with the sample (Fig. 1b, red), with an expected third-order ($n = 2.98 \pm 0.07$) power dependence (Fig. 1c).

For the bare tip response (Fig. 1d, blue), the FWM polarization is parallel to the tip axis, resulting in a purely longitudinal third-order nonlinear antenna current driven by the strong near-field gradients along the tip axis³³. In contrast, the tip-enhanced graphene FWM polarization is in-plane (Fig. 1d, red), with an estimated nanolocalized excitation area as small as $(10 \text{ nm})^2 \pi$, which corresponds to as few as 1×10^4 atoms (see Supplementary Note 1 for details).

We first spatially image and study the graphene FWM layer dependence, as shown in Fig. 1e. A strong and generally homogeneous response is observed within the graphene sheet, with intensity increasing with the number of layers N following a quadratic dependence $I_{\text{FWM}} \propto N^2$ as shown in Fig. 1f^{15,19,20}. This dependence is derived from the third-order nonlinear polarization

$$P^{(3)}(\omega_{\text{FWM}}) = L(\omega_{\text{FWM}}) \chi_{\text{ML}}^{(3)}(\omega_{\text{FWM}}) NL^{(3)}(\omega) E^3(\omega)$$
, where $E(\omega)$ is the excitation field, $\chi_{\text{ML}}^{(3)}(\omega_{\text{FWM}})$ is the surface (2D) third-order nonlinear susceptibility of monolayer graphene, $L(\omega_{\text{FWM}})$ is the local field enhancement factor for FWM and $L(\omega)$ is the local field enhancement factor for excitation frequency, and holds for up to a few layers

¹Department of Physics, Department of Chemistry and JILA, University of Colorado, Boulder, CO, USA. ²Center for Experiments on Quantum Materials, University of Colorado, Boulder, CO, USA. ³ITMO University, Saint Petersburg, Russia. ⁴Institute of Applied Physics, Russian Academy of Sciences, Nizhny Novgorod, Russia. ⁵Department of Physics and Astronomy, Texas A&M University, College Station, TX, USA. *e-mail: belyanin@physics.tamu.edu; markus.raschke@colorado.edu

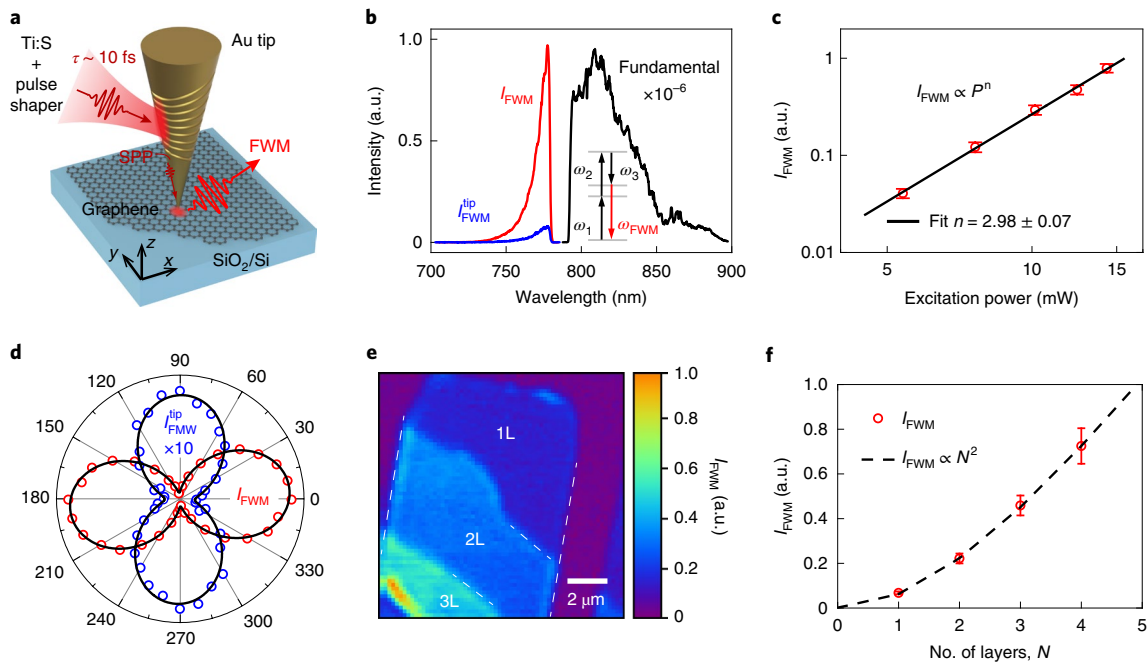


Fig. 1 | Graphene FWM nanoimaging. **a**, Schematic of grating-coupling and femtosecond adiabatic nanofocusing combined with pulse shaping for nanolocalized FWM excitation. **b**, Near-field graphene FWM (I_{FWM}) (red) and free-standing tip FWM ($I_{\text{FWM}}^{\text{tip}}$) (blue) as reference, excited by the fundamental field at the tip apex (black), with a representative FWM pathway indicated. **c**, Power dependence of I_{FWM} (red circles) with fit (black line) indicating third-order power dependence. **d**, Normalized polarization dependence of I_{FWM} (red) and $I_{\text{FWM}}^{\text{tip}}$ (blue, magnified $\times 10$), fitted by a $\cos^2\theta$ dependence. The small angular offset of $\sim 6^\circ$ between the tip and the graphene FWM is probably due to slight structural asymmetry or tilt of the tip. **e**, Near-field FWM imaging of single- and few-layer graphene (the dashed white line indicates the physical graphene edge; Supplementary Fig. 13). **f**, Thickness dependence of the integrated FWM signal I_{FWM} and model fit based on $I_{\text{FWM}} \propto N^2$. Error bars in **c** and **f** are the s.d. calculated from the intensity noise of the signal.

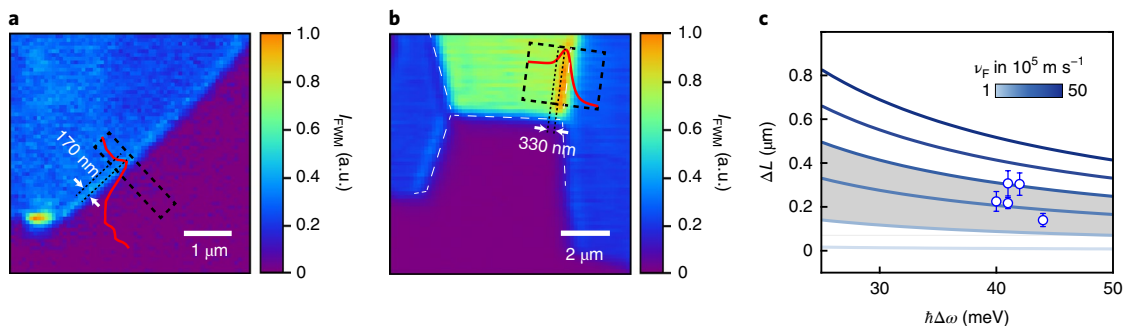


Fig. 2 | Non-locality of the FWM response in graphene. **a,b**, Near-field imaging of monolayer (**a**) and folded (**b**) graphene with line-cuts (red) extracted from signal averaging along the edge-parallel direction (across the rectangular box). Spatial delocalization extracted from the FWM signal rises from 10% to 90%, with value ranging from ~ 170 nm (**a**) to ~ 330 nm (**b**), far exceeding the ~ 10 nm nominal tip near-field spatial resolution. The dashed white line indicates the physical graphene edge (Supplementary Fig. 13). **c**, Length scale ΔL of delocalization as a function of Fermi velocity ν_F and spectral width $\Delta\omega$, determined from the measured FWM spectrum, with spectral variations between different measurements determined by the details of the grating coupling: experimental values, blue circles; model expectations $\Delta L \approx 2\pi\nu_F/\Delta\omega$, line series. Grey shaded area, range of typical ν_F values from 8.5×10^5 to 30×10^5 m s^{-1} (ref. 49). Error bars indicate 1 s.d. calculated from the variation of ΔL along each edge.

as long as the reflection and absorption are small. No significant FWM response is observed from the bare SiO_2/Si substrate.

Notably different from the homogeneous FWM response within the graphene sheet is a generally larger FWM intensity emerging at structural heterogeneities in the form of strained regions, defects, folds and edges. In particular, we consistently observe an enhanced near-field FWM signal along edges, both in single- and multilayer graphene (Fig. 2a,b). The spatial extent of the enhanced signal ranges from ~ 110 to ~ 370 nm, as determined from a wider range

of edges studied (the results are summarized in Fig. 2c), and in all cases exceeds the otherwise nanometre-scale near-field localization by as much as 10 times (for additional data see Supplementary Fig. 2). The near-edge enhanced FWM signal peaks inside at a distance of approximately hundreds of nanometres from the actual graphene edge.

Figure 3a shows an unpolarized FWM image of a monolayer graphene sheet with distinct anisotropy between the edges, with corresponding polarization-resolved imaging under s (tip-perpendicular,

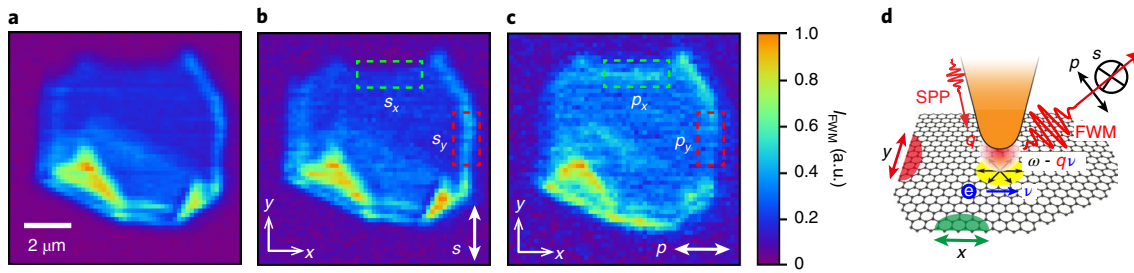


Fig. 3 | Polarization distribution of near-field FWM in graphene. **a**, Unpolarized FWM image of monolayer graphene. **b, c**, Normalized FWM images under *s*- and *p*-polarized detection with edge contrast reversal of I_{FWM} (the higher noise in **c** is due to the approximately seven times lower FWM collection efficiency under *p* compared to *s* polarization). **d**, Schematic of symmetry breaking with destructive FWM source polarization interference (yellow) and lifted degeneracy at the edges (green and red semicircles). The non-locality of FWM is attributed to high near-field momenta q driven by Doppler-shifted frequencies $\omega \rightarrow \omega - qv$.

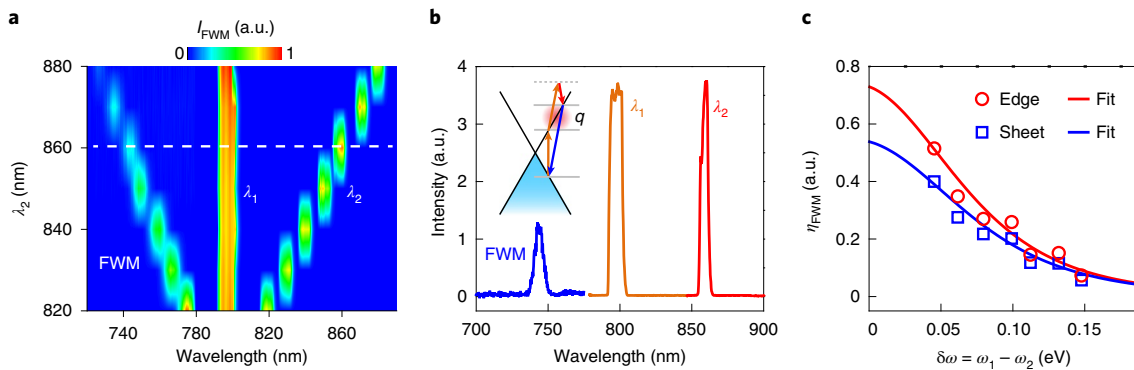


Fig. 4 | FWM nanospectroscopy. **a, b**, FWM dependence on variable λ_2 for fixed $\lambda_1 = 795$ nm (**a**) and example spectra (**b**) for $\lambda_1 = 795$ nm and $\lambda_2 = 860$ nm, as indicated by the white dashed line in **a**. Inset in **b**, one of the dominant FWM processes resonantly driven by large near-field momenta q from the tip (Supplementary Fig. 3). **c**, FWM spectral efficiency as a function of detuning ($\delta\omega$), extracted from **a**, for a graphene sheet and edge, with corresponding fits based on equation (1).

Fig. 3b) and *p* (tip-parallel, Fig. 3c) polarizations (the polarization configurations are depicted in Fig. 3d). From the observation that edges perpendicular to the emitted *k*-vector direction are predominantly enhanced (Fig. 3a,b), and that the polarization contrast is reversed depending on the edge orientation (Fig. 3c), the spatial FWM source polarization vector at the edges is revealed to be oriented parallel with respect to the edges (for details, see Supplementary Note 4).

In general, as shown in Fig. 3d (yellow), for the ideal case of a radially symmetric FWM graphene excitation by the apex SPP near-field, there would be no net radiating FWM polarization because of destructive local interference of the induced FWM nonlinear source polarization. However, even a slight structural asymmetry of the apex, together with retardation effects, give rise to a tip-induced graphene FWM signal with in-plane polarization. The broken symmetry at the graphene edges then further lifts the degeneracy, resulting in the observed FWM edge enhancement.

FWM dependence on detuning frequency

To extract the local relaxation dynamics, we study the FWM process as a function of excitation frequency detuning $\delta\omega = \omega_1 - \omega_2$. As shown in Fig. 4a, the FWM response at $\omega_{\text{FWM}} = 2\omega_1 - \omega_2$ is probed by fixing $\lambda_1 = 795$ nm and varying λ_2 from 820 to 880 nm in steps of 10 nm; example spectra are shown in Fig. 4b. We quantify the FWM intensity dependence on detuning $\delta\omega$ by the FWM efficiency η_{FWM} defined as the ratio of the measured FWM intensity I_{FWM} and reference FWM intensity I_{ref} , calculated from the fundamental tip scattering spectra assuming a flat spectral phase for a

frequency-independent FWM response³³. A pronounced increase in η_{FWM} with decreasing $\delta\omega$ is observed for both the graphene sheet and edge (Fig. 4c).

This behaviour can be modelled based on the frequency detuning dependence of the third-order nonlinear susceptibility with $\eta_{\text{FWM}}(\delta\omega) \propto |\chi^{(3)}(\delta\omega)|^2$. Near the Dirac points in the electric-dipole approximation and in the high-frequency limit, when all frequencies are larger than the Fermi energy, and assuming that all fields are polarized in the *x* direction, $\chi^{(3)}$ is given by^{35,36}

$$\chi_{xxxx}^{(3)}(2\omega_1 - \omega_2; \omega_1, \omega_1, -\omega_2) = \frac{i\sigma_{xxxx}^{(3)}}{2\omega_1 - \omega_2} = \frac{ie^4 v_F^2}{8\hbar^3 \omega_1 (\omega_1 - \omega_2)^2 (2\omega_1 - \omega_2)^2} \quad (1)$$

with the same frequency dependence for all non-zero components of the $\hat{\chi}^{(3)}$ tensor. We include dephasing with characteristic time T_2 in the equations for the off-diagonal density matrix elements. This adds an imaginary part to the smallest term in the frequency denominator $\omega_1 - \omega_2 \rightarrow \omega_1 - \omega_2 + i\Gamma$, with $\Gamma = 1/T_2$. Fitting the data in Fig. 4c to the resulting Lorentzian $\eta_{\text{FWM}}(\delta\omega) \propto |\chi^{(3)}(\delta\omega)|^2$, we obtain $T_2 = 5.2 \pm 0.2$ fs for the spectral edge response (red) and $T_2 = 4.8 \pm 0.2$ fs for the graphene sheet (blue), respectively.

Ultrafast spatio-temporal imaging

Spatial heterogeneity is observed in the static FWM images (Supplementary Fig. 2), possibly due to strain or defects. We explore

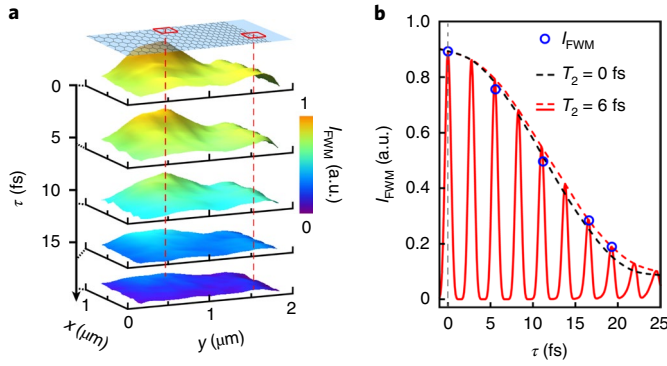


Fig. 5 | Femtosecond spatio-temporal FWM imaging. **a**, 3D rendered FWM images of graphene with two-pulse excitation, corresponding to five inter-pulse delays (from top to bottom), $\tau = 0, 5.6, 11.2, 16.6$ and 19.3 fs. The cartoon on top shows the location of the graphene sheet, with its edge on the right side. **b**, The FWM intensity of the graphene edge (right red square in **a**) for the five delay times (blue circles) shows a finite decoherence time of $T_2 = 6 \pm 1$ fs (red line and red dashed envelope), compared to a simulated instantaneous response (black trace envelope). For corresponding FWM dynamics of the graphene sheet see Supplementary Fig. 5b.

the associated effects on the dephasing time T_2 in corresponding femtosecond spatio-temporal FWM nanoimaging. We use two-pulse excitation and vary the inter-pulse delay τ from 0 to ~ 20 fs, with the resulting FWM images for selected delays shown in Fig. 5a. This spatio-temporal imaging provides for a direct visualization of the FWM decoherence and associated electron dynamics in graphene, as well as its spatial heterogeneity at edges and within the sheet. As can be seen, both non-local edge and spatially heterogeneous sheet responses decay within 20 fs. We find no discernible spatial variation in T_2 within the ± 1 fs uncertainty of the measurement, averaging 200×200 nm² voxels, as needed for adequate signal-to-noise ratio. Compared to the simulation (Supplementary Fig. 5a) based on an instantaneous FWM response $T_2 = 0$ fs, as shown in Fig. 5b (black dashed line), the slight temporal broadening of the FWM intensity averaged along the edge (blue circles) is described by a dephasing time of $T_2 = 6 \pm 1$ fs, which is in agreement with the frequency-domain results above.

This extremely short dephasing time is consistent with results from related studies^{37–39} and can be attributed to efficient and only weakly screened carrier–carrier scattering with rapid energy and momentum redistribution via impact ionization and Auger recombination^{37–41}. Furthermore, at very early times, the interband singularity coupling near the Dirac points responsible for the strong dephasing-induced non-adiabatic and irreversible electron dynamics¹², as well as the dephasing interaction with the coherent Landau–Zener transitions^{43,44}, may need to be considered. Note that at these extremely short timescales and despite tip–sample distances of a few nanometres, near-field polarization transfer and tip–sample coupling only negligibly disturb the intrinsic graphene FWM decoherence⁴⁵. For the nanofocused excitation with an estimated fluence of $\sim 0.7 \pm 0.4$ mJ cm^{−2} at the graphene, a photoexcited carrier density of $\sim 10^{13}–10^{14}$ cm^{−2} is expected. However, the associated excitation-induced dephasing^{46,47} is probably limited, because of the already intrinsically large phase space for carrier–carrier scattering.

Theoretical understanding of non-local effects

The spatial broadening and non-local FWM response at the edges (for control experiments see Supplementary Fig. 8) suggests a new nonlinear mechanism based on Doppler broadening as a combined effect of the unusually high electron Fermi velocity in graphene

together with the high near-field momenta of the tip apex field (for details, see Supplementary Note 5). A similar non-local effect has been observed in the linear optical interaction between electrons and propagating plasmons in graphene⁴⁸. The broad distribution of near-field wavevectors \mathbf{q} (Fig. 3d) generated at the tip apex can make both the linear and nonlinear responses of graphene significantly non-local with $\chi^{(3)}(\mathbf{q})$.

Although a rigorous theory of the third-order nonlinear response of graphene including spatial dispersion is still lacking, the effect of a small tip radius and correspondingly large wavenumbers of the nanofocused pump fields on the third-order nonlinear response of graphene can be estimated qualitatively (for details, see Supplementary Note 15). From the general hierarchy of the density matrix equations solved by the method of successive perturbations, the density matrix element ρ_{mn} in the α th order of perturbation is given by⁸

$$\rho_{mn}^{(\alpha)} = \frac{F(\rho_{pq}^{(\alpha-1)}, \dots, \rho_{pq}^{(1)})}{\omega^{(\alpha)} - \frac{E_m - E_n}{\hbar} + i\Gamma} \quad (2)$$

where the numerator depends on the density matrix elements found in previous orders of perturbation, $E_m(\mathbf{k}_m)$ and $E_n(\mathbf{k}_n)$ are the energies of the electron states connected by optical transitions, and $\omega^{(2)} = \omega_1 \pm \omega_2$ and $\omega^{(3)} = \omega_1 \pm \omega_2 \pm \omega_3$. The energy difference $(E_m - E_n)/\hbar$ in equation (2) can then be expanded in powers of $\mathbf{q}^{(\alpha)}$ as $\omega_{mn} + \mathbf{q}^{(\alpha)} \partial E_m / (\hbar \partial \mathbf{k})$, where $\omega_{mn} = (E_m(\mathbf{k}_m) - E_n(\mathbf{k}_n))/\hbar$ is the transition frequency between states neglecting the change in electron momentum, and the quantity $\mathbf{q}^{(\alpha)} \partial E_m / (\hbar \partial \mathbf{k})$ describes a Doppler shift of the frequency. Here, near-field wavevectors $\mathbf{q}^{(2)} = \mathbf{q}_1 \pm \mathbf{q}_2$, $\mathbf{q}^{(3)} = \mathbf{q}_1 \pm \mathbf{q}_2 \pm \mathbf{q}_3$ and so on. As one can see from comparing equation (2) with equation (1), frequencies in resonant denominators acquire extra Doppler broadening factors $\sim \nu_F q^{(\alpha)}$, where we replaced $\partial E_m / (\hbar \partial \mathbf{k})$ with the characteristic speed ν_F of electrons in graphene. This factor is most important in the terms that originate from second-order corrections and contain the smallest frequencies:

$$\rho_{mn}^{(2)} \propto \frac{1}{\Delta\omega + i\Gamma - \nu_F q^{(2)}} \quad (3)$$

where $\Delta\omega$ is either the frequency difference $\omega_1 - \omega_2$ of two quasi-monochromatic pump fields or the frequency width of the broadband pump field. Even for a very broad wavevector spectrum of the near-field at the tip apex, reaching maximum values of $q_{\max} \approx 2\pi/R > \Delta\omega/\nu_F$, the contributions of the field spatial harmonics with $q > \Delta\omega/\nu_F$ to the nonlinear signal intensity will be suppressed as $1/q^2$. Therefore, the wavevector spectrum of the nonlinear signal will be determined by the harmonics with a maximum value of $q \approx \Delta\omega/\nu_F$. This gives rise to a non-locality of the FWM response and limits the spatial resolution to scales of order $\Delta L \approx 2\pi\nu_F/\Delta\omega$. For a bandwidth of $\hbar\Delta\omega \sim 40$ meV of our FWM signal, and $\nu_F = 10^6$ m s^{−1}, $\Delta L \approx 100$ nm. In good agreement with this theoretical estimate, our measured length scale of FWM delocalization, as shown in Fig. 2c (blue circles), falls within the range of theoretically expected values based on the range of typical reported values of ν_F (ref. 49). The effect might be particularly pronounced in graphene due to the high velocity ν_F of all interacting electrons. However, similar Doppler effects on the nonlinear response are expected for a range of other materials with high-group-velocity electrons. With details depending on band dispersion, this would call for the development of a full theory of non-local third-order nonlinear optics.

Conclusions

In summary, we have performed FWM nanoimaging of graphene, based on adiabatic plasmonic nanofocusing as an enabling technique for femtosecond nanolocalization and nanoimaging.

The FWM spectral and spatio-temporal response provides the first real-time view into the few-femtosecond electronic dephasing underlying the role of different scattering and relaxation pathways, the associated many-body interactions and the possible roles of different heterogeneities, possibly separable in ultrafast coherent nanoimaging. It further reveals the importance of non-local effects in the nonlinear interaction of graphene with spatially localized fields of high momenta, providing a perspective for qualitatively new and distinct nonlinear processes in nonlinear nanooptics with confined fields and with 2D materials. Perhaps most importantly, our approach demonstrates the feasibility of near-field nonlinear studies of nanoscale volumes, in which an increase in the nonlinear signal due to nanofocusing and near-field enhancement overcompensates a decrease in the interaction volume. This enables further advances in the nonlinear nanooptics of 2D materials and their nanostructures, and eventually the development of ultracompact nonlinear optical devices.

Online content

Any methods, additional references, Nature Research reporting summaries, source data, statements of code and data availability and associated accession codes are available at <https://doi.org/10.1038/s41565-019-0515-x>.

Received: 11 December 2018; Accepted: 25 June 2019;

Published online: 05 August 2019

References

- Mikhailov, S. A. Non-linear electromagnetic response of graphene. *Europhys. Lett.* **79**, 27002 (2007).
- Glazov, M. M. & Ganichev, S. D. High frequency electric field induced nonlinear effects in graphene. *Phys. Rep.* **535**, 101–138 (2014).
- Nair, R. R. et al. Fine structure constant defines visual transparency of graphene. *Science* **320**, 1308 (2008).
- Bonaccorso, F., Sun, Z., Hasan, T. & Ferrari, A. C. Graphene photonics and optoelectronics. *Nat. Photon.* **4**, 611–622 (2010).
- Liu, M. et al. A graphene-based broadband optical modulator. *Nature* **474**, 64–67 (2011).
- Mak, K. F., Ju, L., Wang, F. & Heinz, T. F. Optical spectroscopy of graphene: from the far infrared to the ultraviolet. *Solid State Commun.* **152**, 1341–1349 (2012).
- Sun, Z., Martinez, A. & Wang, F. Optical modulators with 2D layered materials. *Nat. Photon.* **10**, 227–238 (2016).
- Wang, Y., Tokman, M. & Belyanin, A. Second-order nonlinear optical response of graphene. *Phys. Rev. B* **94**, 195442 (2016).
- Cheng, J. L., Vermeulen, N. & Sipe, J. E. Second order optical nonlinearity of graphene due to electric quadrupole and magnetic dipole effects. *Sci. Rep.* **7**, 43843 (2017).
- Constant, T. J., Hornett, S. M., Chang, D. E. & Hendry, E. All-optical generation of surface plasmons in graphene. *Nat. Phys.* **12**, 124–127 (2016).
- Bykov, A. Y., Murzina, T. V., Rybin, M. G. & Obraztsova, E. D. Second harmonic generation in multilayer graphene induced by direct electric current. *Phys. Rev. B* **85**, 121413 (2012).
- An, Y. Q., Nelson, F., Lee, J. U. & Diebold, A. C. Enhanced optical second-harmonic generation from the current-biased graphene/SiO₂/Si(001) structure. *Nano Lett.* **13**, 2104–2109 (2013).
- Cheng, J. L., Vermeulen, N. & Sipe, J. E. DC current induced second order optical nonlinearity in graphene. *Opt. Express* **22**, 15868–15876 (2014).
- Shan, Y. et al. Stacking symmetry governed second harmonic generation in graphene trilayers. *Sci. Adv.* **4**, eaat0074 (2018).
- Hendry, E., Hale, P. J., Moger, J., Savchenko, A. K. & Mikhailov, S. A. Coherent nonlinear optical response of graphene. *Phys. Rev. Lett.* **105**, 097401 (2010).
- Gu, T. et al. Regenerative oscillation and four-wave mixing in graphene optoelectronics. *Nat. Photon.* **6**, 554–559 (2012).
- Ciesielski, R. et al. Graphene near-degenerate four-wave mixing for phase characterization of broadband pulses in ultrafast microscopy. *Nano Lett.* **15**, 4968–4972 (2015).
- Jiang, T. et al. Gate-tunable third-order nonlinear optical response of massless Dirac fermions in graphene. *Nat. Photon.* **12**, 430–436 (2018).
- Kumar, N. et al. Third harmonic generation in graphene and few-layer graphite films. *Phys. Rev. B* **87**, 121406 (2013).
- Hong, S.-Y. et al. Optical third-harmonic generation in graphene. *Phys. Rev. X* **3**, 021014 (2013).
- Säynätjoki, A. et al. Rapid large-area multiphoton microscopy for characterization of graphene. *ACS Nano* **7**, 8441–8446 (2013).
- Woodward, R. I. et al. Characterization of the second- and third-order nonlinear optical susceptibilities of monolayer MoS₂ using multiphoton microscopy. *2D Mater.* **4**, 011006 (2017).
- Soavi, G. et al. Broadband, electrically tunable third-harmonic generation in graphene. *Nat. Nanotechnol.* **13**, 583–588 (2018).
- Yoshikawa, N., Tamaya, T. & Tanaka, K. High-harmonic generation in graphene enhanced by elliptically polarized light excitation. *Science* **356**, 736–738 (2017).
- Hafez, H. A. et al. Extremely efficient terahertz high-harmonic generation in graphene by hot Dirac fermions. *Nature* **561**, 507–511 (2018).
- Cox, J. D., Silveiro, I. & García de Abajo, F. J. Quantum effects in the nonlinear response of graphene plasmons. *ACS Nano* **10**, 1995–2003 (2016).
- Cox, J. D. & García de Abajo, F. J. Plasmon-enhanced nonlinear wave mixing in nanostructured graphene. *ACS Photon.* **2**, 306–312 (2015).
- Cox, J. D., Marini, A. & García de Abajo, F. J. Plasmon-assisted high-harmonic generation in graphene. *Nat. Commun.* **8**, 14380 (2017).
- Savostianova, N. A. & Mikhailov, S. A. Giant enhancement of the third harmonic in graphene integrated in a layered structure. *Appl. Phys. Lett.* **107**, 181104 (2015).
- Berweger, S., Atkin, J. M., Xu, X. G., Olmon, R. L. & Raschke, M. B. Femtosecond nanofocusing with full optical waveform control. *Nano Lett.* **11**, 4309–4313 (2011).
- Berweger, S., Atkin, J. M., Olmon, R. L. & Raschke, M. B. Light on the tip of a needle: plasmonic nanofocusing for spectroscopy on the nanoscale. *J. Phys. Chem. Lett.* **3**, 945–952 (2012).
- Kravtsov, V., Ulbricht, R., Atkin, J. M. & Raschke, M. B. Plasmonic nanofocused four-wave mixing for femtosecond near-field imaging. *Nat. Nanotechnol.* **11**, 459–464 (2016).
- Kravtsov, V. et al. Enhanced third-order optical nonlinearity driven by surface-plasmon field gradients. *Phys. Rev. Lett.* **120**, 203903 (2018).
- Tomita, K., Kojima, Y. & Kannari, F. Selective coherent anti-Stokes Raman scattering microscopy employing dual-wavelength nanofocused ultrafast plasmon pulses. *Nano Lett.* **18**, 1366–1372 (2018).
- Cheng, J. L., Vermeulen, N. & Sipe, J. E. Third order optical nonlinearity of graphene. *New J. Phys.* **16**, 53014 (2014).
- Mikhailov, S. A. Quantum theory of the third-order nonlinear electrodynamic effects of graphene. *Phys. Rev. B* **93**, 085403 (2016).
- Winzer, T., Knorr, A. & Malic, E. Carrier multiplication in graphene. *Nano Lett.* **10**, 4839–4843 (2010).
- Xing, G., Guo, H., Zhang, X., Sum, T. C. & Huan, C. H. A. The physics of ultrafast saturable absorption in graphene. *Opt. Express* **18**, 4564–4573 (2010).
- Brida, D. et al. Ultrafast collinear scattering and carrier multiplication in graphene. *Nat. Commun.* **4**, 1987 (2013).
- Tani, S., Blanchard, F. & Tanaka, K. Ultrafast carrier dynamics in graphene under a high electric field. *Phys. Rev. Lett.* **109**, 166603 (2012).
- Huang, D. et al. Gate switching of ultrafast photoluminescence in graphene. *Nano Lett.* **18**, 7985–7990 (2018).
- Kelardeh, H. K., Apalkov, V. & Stockman, M. I. Graphene in ultrafast and superstrong laser fields. *Phys. Rev. B* **91**, 045439 (2015).
- Higuchi, T., Heide, C., Ullmann, K., Weber, H. B. & Hommelhoff, P. Light-field-driven currents in graphene. *Nature* **550**, 224–228 (2017).
- Heide, C., Higuchi, T., Weber, H. B. & Hommelhoff, P. Coherent electron trajectory control in graphene. *Phys. Rev. Lett.* **121**, 207401 (2018).
- Kravtsov, V., Berweger, S., Atkin, J. M. & Raschke, M. B. Control of plasmon emission and dynamics at the transition from classical to quantum coupling. *Nano Lett.* **14**, 5270–5275 (2014).
- McGuire, J. A., Raschke, M. B. & Shen, Y. R. Electron dynamics of silicon surface states: second-harmonic hole burning on Si(111)-(7×7). *Phys. Rev. Lett.* **96**, 087401 (2006).
- Winzer, T. & Malic, E. The impact of pump fluence on carrier relaxation dynamics in optically excited graphene. *J. Phys. Condens. Matter* **25**, 054201 (2013).
- Lundeberg, M. B. et al. Tuning quantum nonlocal effects in graphene plasmonics. *Science* **357**, 187–191 (2017).
- Hwang, C. et al. Fermi velocity engineering in graphene by substrate modification. *Sci. Rep.* **2**, 590 (2012).

Acknowledgements

T.J., V.K. and M.B.R. acknowledge funding from the US Department of Energy, Office of Basic Sciences, Division of Material Sciences and Engineering, under award no. DE-SC0008807. A.B. and M.B.R. acknowledge additional support from the Air Force Office for Scientific Research through grants nos. FA9550-17-1-0341 and FA9550-14-1-0376. V.K. acknowledges support from ITMO Fellowship. M.T. acknowledges support from the

Ministry of Science and Higher Education of the Russian Federation under contract no. 14.W03.31.0032. The authors thank R. Ernstorfer for valuable discussions and Y. Cai, J. Yan, G. C. Geschwind and M. May for experimental support.

Author contributions

V.K., T.J. and M.B.R. conceived and designed the experiments. T.J. and V.K. conducted the measurements. M.T. and A.B. provided the theory. All authors discussed and interpreted the results. T.J. wrote the manuscript with the help of all authors.

Competing interests

The authors declare no competing interests.

Additional information

Supplementary information is available for this paper at <https://doi.org/10.1038/s41565-019-0515-x>.

Reprints and permissions information is available at www.nature.com/reprints.

Correspondence and requests for materials should be addressed to A.B. or M.B.R.

Peer review information: *Nature Nanotechnology* thanks Andrea Giugni, Themistoklis Sidiropoulos and other, anonymous, reviewer(s) for their contribution to the peer review of this work.

Publisher's note: Springer Nature remains neutral with regard to jurisdictional claims in published maps and institutional affiliations.

© The Author(s), under exclusive licence to Springer Nature Limited 2019

Methods

Sample preparation. The graphene samples were mechanically exfoliated from kish graphite crystals (Graphene Supermarket) onto Si substrates with a 90 nm layer of SiO₂.

Experimental set-up. Femtosecond laser pulses from a Ti:sapphire oscillator (Femtolasers, 10 fs pulse duration, 80 MHz repetition rate, centre wavelength 800 nm) were focused onto the chirped grating structure, fabricated by focused ion beam milling into the shaft of electrochemically etched gold tips⁵⁰ as shown in Fig. 1a. Femtosecond SPPs launched by the grating propagate and adiabatically nanofocus at the tip apex. The emission signal from the tip apex was spatially filtered and detected by a spectrometer ($f=500$ mm, SpectraPro 500i, Princeton Instruments) with a thermoelectrically cooled charge-coupled device (ProEM+: 1600 eXcelon3, Princeton Instruments). Both the phase and amplitude of the excitation pulses were modulated by a dual-mask spatial light modulator (CRi SLM640) in the Fourier plane of a 4f pulse shaper. Second-harmonic generation from the tip apex was used as a feedback signal for multiphoton intrapulse interference phase scans^{30–33}. For the optimized transform-limited excitation pulses in the tip nanofocus, wavelengths below 785 nm were blocked by a hardware mask, and the generated FWM near-field signal was collected by an objective (NA = 0.5)

centred at 65° angle with respect to the tip apex and detected using spectral filtering as described previously^{32,33}.

For near-field imaging, the grating tip was mounted onto a quartz tuning fork with dither piezo drive for shear-force tip–graphene distance control and the sample was scanned by the grating tip with sub-nanometre precision using a three-axis piezo stage (Physik Instrumente, P-517), operated by an AFM controller (RHK Technology, R9plus).

For the measurement of the excitation detuning dependence of the FWM intensity, the two laser pulses at centre wavelengths λ_1 and λ_2 were obtained by spectrally shaping of the original broadband spectrum with a movable double-slit mask in the Fourier plane of the pulse shaper.

Data availability

The data that support the plots within this paper and other findings of this study are available from the corresponding author upon reasonable request.

References

50. Neacsu, C. C. et al. Near-field localization in plasmonic superfocusing: a nanoemitter on a tip. *Nano Lett.* **10**, 592–596 (2010).